Methodology for wave force monitoring of bottom-mounted cylinder using the measurement of the wave surface elevation around the body surface

Jiabin Liu [a,b], Anxin Guo [a,b,*], Hui Li [a,b], Hui Hu [c]

[a] *Key Lab of Structures Dynamic Behavior and Control of the Ministry of Education, Harbin Institute of Technology, Harbin, 150090, China*
[b] *Key Lab of Smart Prevention and Mitigation of Civil Engineering Disasters of the Ministry of Industry and Information Technology, Harbin Institute of Technology, Harbin, 150090, China*
[c] *Department of Aerospace Engineering, Iowa State University, Ames, IA 50011, USA*

HIGHLIGHTS

- The relation of wave action and free surface elevation is formulated with a bottom-mounted cylinder.
- An experiment was performed to validate the efficiency of the estimated method.
- The error induced by the linear assumption is discussed.

ARTICLE INFO

ABSTRACT

This paper presents a methodology to estimate the wave force on a bottom-mounted cylinder using the measured signals of wave surface elevation around the body surface of the cylinder. Based on the potential theory, the formulae are derived in a general manner for bottom-mounted cylinders of arbitrary cross section. Considering the difficulty of decomposing the signal of wave surface elevation measured by wave gauges, a linear estimation method is developed to achieve an approximate estimation of the wave loads on cylinders. A hydrodynamic experiment was conducted on a circular cylinder in a random wave field to validate the effectiveness of the proposed method. The horizontal wave forces and bending moments directly measured by force balance are employed for the validation of the proposed estimated results using the measurement of the wave surface elevation by wave gauges. Error analysis is also conducted in the frequency domain to investigate the effects of the linear approximation. The analysis results indicate that the proposed method can effectively estimate the wave loads acting on the cylinder. The linear approximation method slightly underestimates the wave loads of the difference-frequency component, while overestimating that in the sum-frequency region.

1. Introduction

A cylinder is a widely used structural component in coastal and offshore engineering, such as wind turbines, oil platforms and bridges. In a hostile marine environment, the water wave is a primary natural hazard that threatens the safety of the

coastal structures. Understanding the wave–structure interaction mechanism and establishing an appropriate method for estimating the wave loads is fundamentally important for ensuring the safety of the structures.

For a small-scale cylinder, Morison et al. (1950) proposed a semi-empirical method, the so-called Morison equation, for calculating the inline wave force on structure in oscillatory flow. The Morison equation is composed of an inertial force in phase with the local flow acceleration and a drag force proportional to the square of the instantaneous flow velocity. When the diameter of cylinder becomes large, an obvious disturbance on the incident wave, which is generally called diffraction, becomes obvious. In such case, two dimensionless quantities, D/L and KC, are typically used to distinguish the flow regimes of diffraction (Isaacson, 1979), where D is the characteristic length of the cross-section, L is the wave length, and KC is the Keulegan–Carpenter number (Keulegan and Carpenter, 1956). It was found that the diffraction effect cannot be neglected when the ratio of D/L becomes larger than 0.2. In addition, the KC number should be less than the value of $0.44/(D/L)$ to prevent wave breaking. With these conditions, using potential theory, MacCamy and Fuchs (1954) formulated a linear solution for the diffraction problem of a regular wave around a large-scale bottom mounted cylinder.

Compared with a regular wave, a random wave more commonly appears in the ocean environment. When an offshore structure sustains the attack of random waves, the prediction of the wave load acting on the cylinders becomes more complex. Previous works attempted to extend the Morison equation from the condition of regular waves to random waves (Borthwick, 1989; Burrows et al., 1997; Li et al., 1997; Tung, 1996). Recently, Boccotti et al. (2012) conducted a comparison between the in-site measured wave force and the prediction results using the Morison equation acting on a vertical cylinder in a random wave field. In that study, the inertia and drag coefficients for the Morison equation were written as functions of the KC number and the Reynolds (Re) number to improve the accuracy of estimation. Lotfollahi-Yaghin et al. (2012) used an approach based on artificial neural network (ANN) to establish the predictive relationship between the hydrodynamic inline force and the wave surface elevation on a vertical cylinder. The advantage of the ANN method is that it is a model-free method. The results indicated that the predicted results of using ANN matched well with that of Morison equation.

With the application of a structural health monitoring technique in coastal engineering, such as an ocean wind turbine and an offshore platform (Hosseinlou and Mojtahedi, 2016; Jamalkia et al., 2016; Martinez-Luengo et al., 2016; Mojtahedi et al., 2011), the real-time estimation of the wind and wave loads becomes an important issue to assess the structural safety with the in-situ measured data. Although some theoretical methods have been developed for calculating the wave loads, those methods have some limitations for real-time estimation of the wave force, including: (1) because most of the theoretical methods were developed based on the regular wave action, in a random wave field, they are always not effective for computing the wave force; (2) the wave properties of the un-disturbed wave field, such as wave height and wave period, should be known. However, on the site of the structure, it is always difficult to measure the un-disturbed wave properties because of the influence of the structure, especially for multi-body cases, which contains the scattering wave and radiation wave from other bodies.

For large-scale structures, the previous studies (Chan et al., 1995; De Vos et al., 2007; Deng et al., 2016; Li et al., 2012, 2014; Niedzwecki and Duggal, 1992) found that there exists a correlation between the wave run-up and the wave force. Based on this conclusion, it is possible to determine a method to monitor the wave force acting on the cylindrical bodies through measurement of the wave surface elevation around the cylinders. Based on this philosophy, this paper presents a methodology to estimate the wave force of bottom-mounted cylinders by the measured data of wave gauges around the body surface. The main contents of this study are organized into three sections. First, the definition of the physical problem and the methodology for the wave load estimation are presented in §2. Next, a linear estimation method for the wave loads is introduced in §3 by using the recorded data of wave surface elevation around the cylinders. To validate the effectiveness of the proposed method, the results of a hydrodynamic experiment performed with a circular cylinder under random wave field is presented in §4. Finally, the main findings of the present work are summarized.

2. Methodology

Simulation of the wave–structure interaction, which is a very complicated physical phenomenon, is a difficult problem. To make the problem manageable, several assumptions were made to simplify the analysis (Sarpkaya, 2010), including:

(1) the fluid is inviscid and incompressible;

(2) the flow is unseparated around the solid structure;

(3) the effects of surface tension, dissolved gases, cavitation, density and temperature gradients of the water are negligible;

(4) the cylinder is rigid and bottom-mounted at the seabed with uniform shape.

Under the action of the gravity waves, the flow field can be represented by a scalar velocity potential. Without loss of generality, the rigid body is assumed to have an arbitrary cross-section with smooth surface. For the convenience of analysis, a rectangular and a polar coordinate are defined, as shown in Fig. 1. For the two coordinate systems, the $x - y$ or $r - \theta$ planes are all set at the still water level (SWL), and the origin is inside the cross-section of the cylinder. The z-axis is perpendicular to the SWL and positive upward.

The following derivation was formulated for the cylinder whose cross-section is arbitrary and can be represented by a Fourier series. The radius function, $r(\theta)$, of the cross-section in the polar coordinate was then written in the following form
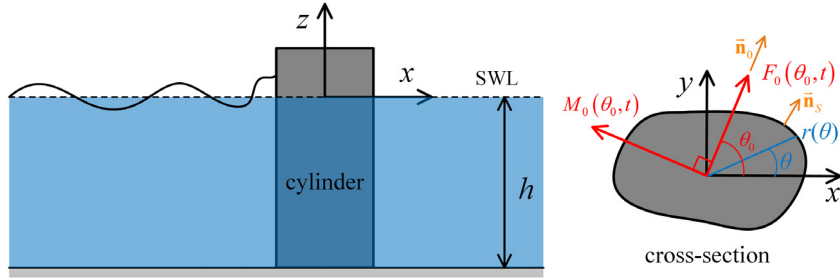
Fig. 1. Definition of the physical problem.

with the Fourier expansion

$$r(\theta) = \sum_{n_r=-\infty}^{\infty} b_{n_r} e^{in_r\theta} \tag{1}$$

where b_{n_r} are the Fourier coefficient of radius function, and $n_r \in Z$. Thus, the surface function, S, for the cross-section can be given by

$$S(r,\theta) = r - \sum_{n_r=-\infty}^{\infty} b_{n_r} e^{in_r\theta} \tag{2}$$

The wave surface elevation around the structure can be represented by the velocity potential as

$$\eta(\theta, t) = -\frac{1}{g}\mathrm{Re}\left\{\frac{\partial\Phi}{\partial t}\Big|_{z=\eta,S=0}\right\} - \frac{1}{2g}\mathrm{Re}\left\{\nabla\Phi\,|_{z=\eta,S=0}\right\} \cdot \mathrm{Re}\left\{\nabla\Phi|_{z=\eta,S=0}\right\} \tag{3}$$

where Φ is the complex-form velocity potential around the cylinder; g is the gravity acceleration. According to the Bernoulli equation, the pressure on the cylinder can be written as

$$P(r,\theta,z,t) = -\rho gz - \rho\mathrm{Re}\left\{\frac{\partial\Phi}{\partial t}\right\} - \frac{\rho}{2}\mathrm{Re}\left\{\nabla\Phi\right\} \cdot \mathrm{Re}\left\{\nabla\Phi\right\} \tag{4}$$

where ρ is the density of water. Therefore, the resultant force acting on the cylinder by the waves, as shown in Fig. 1, can be calculated by integrating the pressure on the body surface as

$$
\begin{aligned}
F_0(\theta_0, t) &= \int_{S=0}\int_{-h}^{\eta(\theta,t)} P\left(-\vec{\mathbf{n}}_S\right) \cdot \vec{\mathbf{n}}_0 dzds = \int_{S=0}\int_{-h}^{\eta(\theta,t)} P\left(-\vec{\mathbf{n}}_S\right) \cdot \vec{\mathbf{n}}_0 \cdot \widetilde{r}(\theta)dzd\theta \\
&= \int_0^{2\pi}\int_{-h}^{\eta(\theta,t)} \left(-\rho gz - \rho\mathrm{Re}\left\{\frac{\partial\Phi}{\partial t}\right\} - \frac{\rho}{2}\mathrm{Re}\left\{\nabla\Phi\right\} \cdot \mathrm{Re}\left\{\nabla\Phi\right\}\right)\Bigg|_{S=0}\left(-\vec{\mathbf{n}}_S\right) \cdot \vec{\mathbf{n}}_0 \cdot \widetilde{r}(\theta)dzd\theta \\
&= \int_0^{2\pi}\int_{-h}^{\eta(\theta,t)} \left(-\rho\mathrm{Re}\left\{\frac{\partial\Phi}{\partial t}\right\} - \frac{\rho}{2}\mathrm{Re}\left\{\nabla\Phi\right\} \cdot \mathrm{Re}\left\{\nabla\Phi\right\}\right)\Bigg|_{S=0}\left(-\vec{\mathbf{n}}_S\right) \cdot \vec{\mathbf{n}}_0 \cdot \widetilde{r}(\theta)dzd\theta \\
&= F_\xi(\theta_0, t) + F_\zeta(\theta_0, t)
\end{aligned}
\tag{5}
$$

where θ_0 is the angle between the direction of F_0 and x-axis, as shown in Fig. 1; $\vec{\mathbf{n}}_S$ is the unit normal vector on the cylinder surface; $\vec{\mathbf{n}}_0$ is the unit normal vector in the direction of resultant wave force, as shown in Fig. 1; h is the water depth; $\widetilde{r}(\theta)$ is a function of θ, which has the following relationship with the radius function

$$\widetilde{r}(\theta) = \sqrt{\left(\frac{dr(\theta)}{d\theta}\right)^2 + (r(\theta))^2} \tag{6}$$

Similar to the resultant wave force, the resultant bending moment at the cylindrical base can also be written as

$$
\begin{aligned}
M_0(\theta_0, t) &= \int_{S=0}\int_{-h}^{\eta(\theta,t)} P(h+z)\left(-\vec{\mathbf{n}}_S\right) \cdot \vec{\mathbf{n}}_0 dzds \\
&= M_\xi(\theta_0, t) + M_\zeta(\theta_0, t) + F_0(\theta_0, t)h
\end{aligned}
\tag{7}
$$

Detailed derivation of Eq. (7) is given in Appendix A.

In Eqs. (5) and (7), the total wave force and base bending moment are separated into two and three terms at the right-hand, respectively, as given by

$$F_\xi\left(\theta_0, t\right) = \int_0^{2\pi} \int_{-h}^{\eta(\theta,t)} \left(-\rho \mathrm{Re}\left\{\frac{\partial \Phi}{\partial t}\right\}\right)\Bigg|_{S=0} \left(-\vec{\mathbf{n}}_S\right) \cdot \vec{\mathbf{n}}_0 \cdot \widetilde{r}(\theta) dz d\theta \tag{8}$$

$$F_\zeta\left(\theta_0, t\right) = \int_0^{2\pi} \int_{-h}^{\eta(\theta,t)} \left(-\frac{\rho}{2}\mathrm{Re}\left\{\nabla\Phi\right\} \cdot \mathrm{Re}\left\{\nabla\Phi\right\}\right)\Bigg|_{S=0} \left(-\vec{\mathbf{n}}_S\right) \cdot \vec{\mathbf{n}}_0 \cdot \widetilde{r}(\theta) dz d\theta \tag{9}$$

$$M_\xi\left(\theta_0, t\right) = \int_0^{2\pi} \int_{-h}^{\eta(\theta,t)} \left(-\rho z \mathrm{Re}\left\{\frac{\partial \Phi}{\partial t}\right\}\right)\Bigg|_{S=0} \left(-\vec{\mathbf{n}}_S\right) \cdot \vec{\mathbf{n}}_0 \cdot \widetilde{r}(\theta) dz d\theta \tag{10}$$

$$M_\zeta\left(\theta_0, t\right) = \int_0^{2\pi} \int_{-h}^{\eta(\theta,t)} \left(-\frac{\rho z}{2}\mathrm{Re}\left\{\nabla\Phi\right\} \cdot \mathrm{Re}\left\{\nabla\Phi\right\}\right)\Bigg|_{S=0} \left(-\vec{\mathbf{n}}_S\right) \cdot \vec{\mathbf{n}}_0 \cdot \widetilde{r}(\theta) dz d\theta \tag{11}$$

For the flow field with random waves, the velocity potential can be expressed by the superposition of linear complex wave potential as

$$\Phi = \sum_{n=1}^{\infty} f_n\left(k_n z\right) g_n\left(k_n, r, \theta, t\right) \tag{12}$$

where k_n is the wave number; $f_n\left(k_n z\right)$ is a real function of z; $g_n\left(k_n, r, \theta, t\right)$ is a complex function of r, θ and t; the real part of the wave potential can be written as

$$\begin{aligned}
\mathrm{Re}\left\{\Phi\right\} &= \sum_{n=1}^{\infty} \mathrm{Re}\left\{f_n\left(k_n z\right) g_n\left(k_n, r, \theta, t\right)\right\} \\
&= \sum_{n=1}^{\infty} f_n\left(k_n z\right) \mathrm{Re}\left\{g_n\left(k_n, r, \theta, t\right)\right\}
\end{aligned} \tag{13}$$

To simplify the notation, the real symbol, Re, of function $g_n\left(\cdot\right)$ is ignored and written as g_n in the following derivation. Substituting Eq. (13) into Eq. (3), the wave surface elevation around the cylinder can be written in the same form as Eq. (5):

$$\eta\left(\theta, t\right) = \eta_\xi\left(\theta, t\right) + \eta_\zeta\left(\theta, t\right) \tag{14}$$

in which

$$\begin{aligned}
\eta_\xi\left(\theta, t\right) &= -\frac{1}{g}\mathrm{Re}\left\{\frac{\partial \Phi}{\partial t}\Bigg|_{z=\eta, S=0}\right\} = \sum_{n=1}^{\infty} \left(-\frac{1}{g} f_n\left(k_n \eta\right) \frac{\partial g_n\left(k_n, r, \theta, t\right)}{\partial t}\right)\Bigg|_{S=0} \\
&= \sum_{n=1}^{\infty} \xi_n\left(\theta, t\right)
\end{aligned} \tag{15}$$

$$\begin{aligned}
\eta_\zeta\left(\theta, t\right) &= -\frac{1}{2g}\mathrm{Re}\left\{\nabla\Phi|_{z=\eta, S=0}\right\} \cdot \mathrm{Re}\left\{\nabla\Phi|_{z=\eta, S=0}\right\} \\
&= \sum_{n=1}^{\infty}\sum_{m=1}^{\infty} -\frac{1}{2g}\left[f_n(k_n\eta)f_m(k_m\eta)(g_n)_r'(g_m)_r' \right. \\
&\quad \left. + \frac{f_n(k_n\eta)f_m(k_m\eta)(g_n)_\theta'(g_m)_\theta'}{r^2} + g_n g_m k_n k_m \dot{f}_n(k_n\eta)\dot{f}_m(k_m\eta)\right]\Bigg|_{S=0} \\
&= \sum_{n=1}^{\infty}\sum_{m=1}^{\infty} \zeta_{nm}\left(\theta, t\right)
\end{aligned} \tag{16}$$

where $\nabla = \frac{\partial}{\partial r}\vec{\mathbf{e}}_r + \frac{1}{r}\frac{\partial}{\partial \theta}\vec{\mathbf{e}}_\theta + \frac{\partial}{\partial z}\vec{\mathbf{e}}_z$; $\xi_n\left(\theta, t\right)$ and $\zeta_{nm}\left(\theta, t\right)$ represent the component of $\eta_\xi\left(\theta, t\right)$ and $\eta_\zeta\left(\theta, t\right)$, respectively, with different n and m; $(\cdot)_r' = \frac{\partial(\cdot)}{\partial r}, (\cdot)_\theta' = \frac{\partial(\cdot)}{\partial \theta}$ and $\dot{f}_n(k_n z) = \frac{df_n(k_n z)}{d(k_n z)}$.

Further substituting Eq. (13) into Eqs. (8) and (10), the first term of the resultant wave force and base bending moment can also be rewritten as

$$
\begin{aligned}
F_\xi(\theta_0, t) &= \sum_{n=1}^{\infty} \int_0^{2\pi} \int_{-h}^{\eta(\theta,t)} \left(-\rho f_n(k_n z) \frac{\partial g_n}{\partial t} \right)\Bigg|_{S=0} \left(-\vec{\mathbf{n}}_S \right) \cdot \vec{\mathbf{n}}_0 \cdot \widetilde{r}(\theta) dz d\theta \\
&= \sum_{n=1}^{\infty} \int_0^{2\pi} \left(-\rho \frac{f_n(k_n \eta) \partial g_n}{\partial t} \right)\Bigg|_{S=0} \lambda_n(\eta) \left(-\vec{\mathbf{n}}_S \right) \cdot \vec{\mathbf{n}}_0 \cdot \widetilde{r}(\theta) d\theta \\
&= \sum_{n=1}^{\infty} \rho g \int_0^{2\pi} \lambda_n(\eta) \xi_n(\theta, t) \left(-\vec{\mathbf{n}}_S \right) \cdot \vec{\mathbf{n}}_0 \cdot \widetilde{r}(\theta) d\theta
\end{aligned}
\tag{17}
$$

$$
\begin{aligned}
M_\xi(\theta_0, t) &= \sum_{n=1}^{\infty} \int_0^{2\pi} \int_{-h}^{\eta(\theta,t)} \left(-\rho z f_n(k_n z) \frac{\partial g_n}{\partial t} \right)\Bigg|_{S=0} \left(-\vec{\mathbf{n}}_S \right) \cdot \vec{\mathbf{n}}_0 \cdot \widetilde{r}(\theta) dz d\theta \\
&= \sum_{n=1}^{\infty} \int_0^{2\pi} \left(-\rho \frac{f_n(k_n \eta) \partial g_n}{\partial t} \right)\Bigg|_{S=0} \vartheta_n(\eta) \left(-\vec{\mathbf{n}}_S \right) \cdot \vec{\mathbf{n}}_0 \cdot \widetilde{r}(\theta) d\theta \\
&= \sum_{n=1}^{\infty} \rho g h \int_0^{2\pi} \vartheta_n(\eta) \xi_n(\theta, t) \left(-\vec{\mathbf{n}}_S \right) \cdot \vec{\mathbf{n}}_0 \cdot \widetilde{r}(\theta) d\theta
\end{aligned}
\tag{18}
$$

where

$$
\lambda_n(\eta) = \frac{\int_{-h}^{\eta(\theta,t)} f_n(k_n z)\, dz}{f_n(k_n \eta)}
\tag{19}
$$

$$
\vartheta_n(\eta) = \frac{1}{h} \frac{\int_{-h}^{\eta(\theta,t)} z f_n(k_n z)\, dz}{f_n(k_n \eta)}
\tag{20}
$$

The second term of the wave force and bending moment, given in Eqs. (9) and (11), can also be given by

$$
F_\zeta(\theta_0, t) = \sum_{n=1}^{\infty} \sum_{m=1}^{\infty} \rho g \int_0^{2\pi} \{ \zeta_{nm}(\theta, t) \alpha_{nm}(\eta) + \delta_{nm}(\eta) \} \left(-\vec{\mathbf{n}}_S \right) \cdot \vec{\mathbf{n}}_0 \cdot \widetilde{r}(\theta) d\theta
\tag{21}
$$

$$
M_\zeta(\theta_0, t) = \sum_{n=1}^{\infty} \sum_{m=1}^{\infty} \rho g h \int_0^{2\pi} \{ \zeta_{nm}(\theta, t) \beta_{nm}(\eta) + \sigma_{nm}(\eta) \} \left(-\vec{\mathbf{n}}_S \right) \cdot \vec{\mathbf{n}}_0 \cdot \widetilde{r}(\theta) d\theta
\tag{22}
$$

where

$$
\alpha_{nm}(\eta) = \frac{\int_{-h}^{\eta(\theta,t)} f_n(k_n z) f_m(k_m z)\, dz}{f_n(k_n \eta) f_m(k_m \eta)}
\tag{23}
$$

$$
\begin{aligned}
\delta_{nm}(\eta) = \frac{g_n g_m k_n k_m}{f_n(k_n \eta) f_m(k_m \eta)} \Bigg[& f_n(k_n \eta) f_m(k_m \eta) \int_{-h}^{\eta(\theta,t)} \dot{f}_n(k_n z) \dot{f}_m(k_m z)\, dz \\
& - \dot{f}_n(k_n \eta) \dot{f}_m(k_m \eta)_z \int_{-h}^{\eta(\theta,t)} f_n(k_n z) f_m(k_m z)\, dz \Bigg]
\end{aligned}
\tag{24}
$$

$$
\beta_{nm}(\eta) = \frac{1}{h} \frac{\int_{-h}^{\eta(\theta,t)} z f_n(k_n z) f_m(k_m z)\, dz}{f_n(k_n \eta) f_m(k_m \eta)}
\tag{25}
$$

$$
\begin{aligned}
\sigma_{nm}(\eta) = \frac{1}{h} \frac{g_n g_m k_n k_m}{f_n(k_n \eta) f_m(k_m \eta)} \Bigg[& f_n(k_n \eta) f_m(k_m \eta) \int_{-h}^{\eta(\theta,t)} z \dot{f}_n(k_n z) \dot{f}_m(k_m z)\, dz \\
& - \dot{f}_n(k_n \eta) \dot{f}_m(k_m \eta) \int_{-h}^{\eta(\theta,t)} z f_n(k_n z) f_m(k_m z)\, dz \Bigg]
\end{aligned}
\tag{26}
$$

Detail derivation of Eqs. (21) and (22) are given in Appendix A. Herein, the term of $\delta_{nm}(\eta)$ and $\sigma_{nm}(\eta)$ are first assumed to be negligible. The induced error will be discussed later in the next section. With Eqs. (17) and (21), the wave force as

described in Eq. (5) can be written as

$$F(\theta_0, t) = \int_0^{2\pi} \rho g \widetilde{\eta}_F \left(-\vec{\mathbf{n}}_S\right) \cdot \vec{\mathbf{n}}_0 \cdot \widetilde{r}(\theta) d\theta \tag{27}$$

where

$$\widetilde{\eta}_F(\theta, t) = \sum_{n=1}^{\infty} \xi_n(\theta, t) \lambda_n(\eta) + \sum_{n=1}^{\infty} \sum_{m=1}^{\infty} \zeta_{nm}(\theta, t) \alpha_{nm}(\eta) \tag{28}$$

Similarly, with Eqs. (18) and (22), the base bending moment described in Eq. (7) can also be written as

$$M(\theta_0, t) = \int_0^{2\pi} \rho g h \widetilde{\eta}_M \left(-\vec{\mathbf{n}}_S\right) \cdot \vec{\mathbf{n}}_0 \cdot \widetilde{r}(\theta) d\theta \tag{29}$$

where

$$\begin{aligned}
\widetilde{\eta}_M(\theta, t) &= \sum_{n=1}^{\infty} \xi_n(\theta, t) \left(\vartheta_n(\eta) + \lambda_n(\eta)\right) \\
&\quad + \sum_{n=1}^{\infty} \sum_{m=1}^{\infty} \zeta_{nm}(\theta, t) \left(\beta_{nm}(\eta) + \alpha_{nm}(\eta)\right)
\end{aligned} \tag{30}$$

3. Calculation of $\widetilde{\eta}_F(\theta, t)$ and $\widetilde{\eta}_M(\theta, t)$

It is observed from the above derivation that the wave action can be estimated if the wave surface elevation around the cylinder can be measured by using the wave gauges. However, how to obtain $\widetilde{\eta}_F(\theta, t)$ and $\widetilde{\eta}_M(\theta, t)$ from the measured $\eta(\theta, t)$ around the cylinder is still a problem. To solve this problem, the component of the potential $g_n(k_n, r, \theta, t)$ in Eq. (12) is first separated in the spatial and time domains as

$$g_n(k_n, r, \theta, t) = \text{Re} \left\{ \widetilde{g}_n(k_n, r, \theta) \cdot e^{-i\omega_n t} \right\} \tag{31}$$

where ω_n is the circular frequency matching the dispersion relationship

$$\omega_n^2 = k_n g \tanh k_n h \tag{32}$$

The product terms of $g_n \cdot g_m$ is then obtained to be

$$\begin{aligned}
g_n \cdot g_m &= \frac{1}{2} \text{Re} \left\{ \widetilde{g}_n(k_n, r, \theta) \widetilde{g}_m(k_m, r, \theta) \cdot e^{-i(\omega_n + \omega_m)t} \right. \\
&\quad \left. + \widetilde{g}_n(k_n, r, \theta) \widetilde{g}_m^*(k_m, r, \theta) \cdot e^{-i(\omega_n - \omega_m)t} \right\}
\end{aligned} \tag{33}$$

where $\widetilde{g}_m^*(\cdot)$ is the conjugate function of $\widetilde{g}_m(\cdot)$.

Substituting Eq. (33) into Eqs. (15) and (16), the equations can be rewritten as

$$\xi_n(\theta, t) = \text{Re} \left\{ A(\cdot) \cdot e^{-i\omega_n t} \right\} \tag{34}$$

$$\zeta_{nm}(\theta, t) = \text{Re} \left\{ B(\cdot) \cdot e^{-i(\omega_n + \omega_m)t} \right\} + \text{Re} \left\{ C(\cdot) \cdot e^{-i(\omega_n - \omega_m)t} \right\} \tag{35}$$

where

$$A(\cdot) \approx i \frac{1}{2} \frac{\omega_n}{g} f_n(k_n \eta) \widetilde{g}_n(k_n, r, \theta) \tag{36}$$

$$\begin{aligned}
B(\cdot) &= -\frac{1}{4g} \left[f_n(k_n\eta)f_m(k_m\eta) \cdot (\widetilde{g}_n)_r'(\widetilde{g}_m)_r' + \frac{f_n(k_n\eta)f_m(k_m\eta)}{r^2} \cdot (\widetilde{g}_n)_\theta'(\widetilde{g}_m)_\theta' \right. \\
&\quad \left. + k_n k_m \dot{f}_n(k_n\eta)\dot{f}_m(k_m\eta) \cdot \widetilde{g}_n \widetilde{g}_m \right]
\end{aligned} \tag{37}$$

$$\begin{aligned}
C(\cdot) &= -\frac{1}{4g} \left[f_n(k_n\eta)f_m(k_m\eta) \cdot (\widetilde{g}_n)_r'(\widetilde{g}_m^*)_r' + \frac{f_n(k_n\eta)f_m(k_m\eta)}{r^2} \cdot (\widetilde{g}_n)_\theta'(\widetilde{g}_m^*)_\theta' \right. \\
&\quad \left. + k_n k_m \dot{f}_n(k_n\eta)\dot{f}_m(k_m\eta) \cdot \widetilde{g}_n \widetilde{g}_m^* \right]
\end{aligned} \tag{38}$$

Next, substituting Eqs. (34) and (35) into Eq. (14), the measured signal of wave surface elevation around the cylinder can be rewritten in the form of

$$
\eta\left(\theta, t\right) = \sum_{n=1}^{\infty} \mathrm{Re}\left\{A\left(\cdot\right) \cdot e^{-i\omega_n t}\right\} + \sum_{n=1}^{\infty}\sum_{m=1}^{\infty} \mathrm{Re}\left\{B\left(\cdot\right) \cdot e^{-i(\omega_n+\omega_m)t}\right\}
$$
$$
+ \sum_{n=1}^{\infty}\sum_{m=1}^{\infty} \mathrm{Re}\left\{C\left(\cdot\right) \cdot e^{-i(\omega_n-\omega_m)t}\right\}
\tag{39}
$$

It is observed from Eq. (39), that the measured wave surface elevation around the cylinder can be decomposed into three terms. Similarly, substituting Eqs. (34) and (35) into Eqs. (28) and (30), the $\widetilde{\eta}_F\left(\theta, t\right)$ and $\widetilde{\eta}_M\left(\theta, t\right)$ can be rewritten as

$$
\widetilde{\eta}_F\left(\theta, t\right) \approx \sum_{n=1}^{\infty} \lambda_n \mathrm{Re}\left\{A\left(\cdot\right) \cdot e^{-i\omega_n t}\right\} + \sum_{n=1}^{\infty}\sum_{m=1}^{\infty} \alpha_{nm}\mathrm{Re}\left\{B\left(\cdot\right) \cdot e^{-i(\omega_n+\omega_m)t}\right\}
$$
$$
+ \sum_{n=1}^{\infty}\sum_{m=1}^{\infty} \alpha_{nm}\mathrm{Re}\left\{C\left(\cdot\right) \cdot e^{-i(\omega_n-\omega_m)t}\right\}
\tag{40}
$$

$$
\widetilde{\eta}_M\left(\theta, t\right) \approx \sum_{n=1}^{\infty} \left(\vartheta_n + \lambda_n\right) \mathrm{Re}\left\{A\left(\cdot\right) \cdot e^{-i\omega_n t}\right\}
$$
$$
+ \sum_{n=1}^{\infty}\sum_{m=1}^{\infty} \left(\beta_{nm} + \alpha_{nm}\right) \mathrm{Re}\left\{B\left(\cdot\right) \cdot e^{-i(\omega_n+\omega_m)t}\right\}
$$
$$
+ \sum_{n=1}^{\infty}\sum_{m=1}^{\infty} \left(\beta_{nm} + \alpha_{nm}\right) \mathrm{Re}\left\{C\left(\cdot\right) \cdot e^{-i(\omega_n-\omega_m)t}\right\}
\tag{41}
$$

From the above-described equation, it can be found that the next step is to derive the coefficients of $\lambda_n\left(\eta\right), \vartheta_{nm}(\eta), \alpha_{nm}(\eta)$ and $\beta_{nm}(\eta)$. It is well known that function of $f_n\left(k_n z\right)$ in Eq. (12) can be given as

$$
f_n\left(k_n z\right) = a_n \cdot \frac{\cosh k_n\left(z + h\right)}{\cosh k_n h}
\tag{42}
$$

The self-product of $f_n\left(k_n z\right)$ and $\dot{f}_n\left(k_n z\right)$ are then obtained as

$$
f_n\left(k_n z\right) \cdot f_m\left(k_m z\right) = a_n a_m \cdot \frac{\cosh k_n\left(z + h\right)}{\cosh k_n h}\frac{\cosh k_m\left(z + h\right)}{\cosh k_m h}
\tag{43}
$$

$$
\dot{f}_n\left(k_n z\right) \cdot \dot{f}_m\left(k_m z\right) = a_n a_m \cdot \frac{\sinh k_n\left(z + h\right)}{\cosh k_n h}\frac{\sinh k_m\left(z + h\right)}{\cosh k_m h}
\tag{44}
$$

Substituting Eq. (42) into Eqs. (19) and (20) with the assumption of $\eta\left(\theta, t\right) \ll h$, the following is obtained:

$$
\lambda_n\left(\eta\right) = \frac{\tanh k_n\left(\eta + h\right)}{k_n} \approx \frac{\tanh k_n h}{k_n}
\tag{45}
$$

$$
\vartheta_n\left(\eta\right) = \frac{\eta}{h k_n}\tanh k_n\left(\eta + h\right) - \frac{1}{h k_n^2} + \frac{1}{h k_n^2}\frac{1}{\cosh k_n\left(\eta + h\right)}
$$
$$
\approx \frac{1}{h k_n^2}\left(\frac{1}{\cosh k_n h} - 1\right)
\tag{46}
$$

Further substituting Eqs. (43) and (44) into Eqs. (23) and (25), the formulae for $\alpha_{nm}\left(\eta\right)$ and $\beta_{nm}\left(\eta\right)$ can be obtained, which can be found in Appendix B.

From the above derivation, it can be found that the following assumptions are utilized: (1) the random incident wave is assumed to be comprised of a series of linear wave, as seen in Eq. (12); (2) the coefficients $\lambda_n\left(\eta\right), \vartheta_{nm}(\eta), \alpha_{nm}(\eta)$ and $\beta_{nm}(\eta)$ are derived based on the condition of $\eta\left(\theta, t\right) \ll h$. However, it can be observed that the estimated wave force and base bending moment shown in Eqs. (27) and (29) still include nonlinear terms caused by the product term of wave potential, despite the linear assumption of the random incident wave. Generally, the function of $\widetilde{g}_n$ is very complex, so that high accuracy decomposition of linear term and nonlinear term of $\eta\left(\theta, t\right)$, as given in Eq. (39), is difficult to obtain. Therefore, an approximate method is developed to calculate the value of $\widetilde{\eta}_F\left(\theta, t\right)$ and $\widetilde{\eta}_M\left(\theta, t\right)$ for estimating the wave action.

In this approximate method, the coefficients α_{nm} and $\beta_{nm} + \alpha_{nm}$ in Eqs. (40) and (41) are replaced by using $\lambda_{\bar{n}}$ and $\vartheta_{\bar{n}} + \lambda_{\bar{n}}$, respectively, which are dependent on the frequency of $\omega_n \pm \omega_m$ as follows:

$$
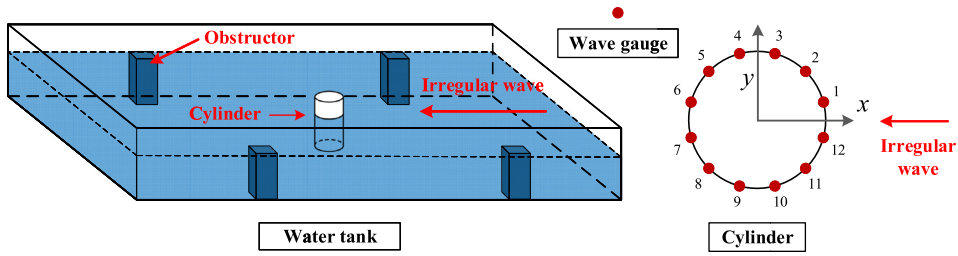\lambda_{\bar{n}} = \frac{\tanh k_{\bar{n}}^{\pm} h}{k_{\bar{n}}^{\pm}}
\tag{47}
$$

Fig. 2. Schematic of experiment setup.

$$\vartheta_{\bar{n}} = \frac{1}{h\left(k_{\bar{n}}^{\pm}\right)^2} \left(\frac{1}{\cosh k_{\bar{n}}^{\pm}h} - 1\right) \tag{48}$$

where frequency $k_{\bar{n}}^{\pm}$ has the relation of $(\omega_n \pm \omega_m)^2 = k_{\bar{n}}^{\pm}g \tanh\left(k_{\bar{n}}^{\pm}h\right)$; $\bar{n}$ is an identifier for the frequency of $\omega_n \pm \omega_m$. Next, in Eqs. (39)–(40), the nonlinear part of $B(\cdot)$ and $C(\cdot)$ can be merged into the linear part of $A(\cdot)$. Therefore, the wave surface elevation around the cylinder can be simplified into the combination of a series of linear components. In such a condition, the measured signal of the wave surface elevation around the cylinder can also be written as the expansion of the Fourier series as

$$\eta(\theta, t) = \sum_{n=1}^{\infty} a_n(\theta) \cos(\omega_n t + \varphi_n(\theta)) \tag{49}$$

where $a_n(\theta)$ and $\varphi_n(\theta)$ are the amplitude and phase corresponding to the frequency of ω_n. Therefore, based on the simplified forms of Eqs. (40) and (41), $\widetilde{\eta}_F(\theta, t)$ and $\widetilde{\eta}_M(\theta, t)$ can be written as

$$\widetilde{\eta}_F(\theta, t) = \sum_{n=1}^{\infty} \frac{\tanh k_n h}{k_n} a_n(\theta) \cos(\omega_n t + \varphi_n(\theta)) \tag{50}$$

$$\widetilde{\eta}_M(\theta, t) = \sum_{n=1}^{\infty} \left(\frac{1}{hk_n^2}\left(\frac{1}{\cosh k_n h} - 1\right) + \frac{\tanh k_n h}{k_n}\right) a_n(\theta) \cos(\omega_n t + \varphi_n(\theta)) \tag{51}$$

The linear estimation of the resultant wave force and base bending moment can be easily obtained after substituting Eqs. (50) and (51) into Eqs. (27) and (29).

4. Experimental validation

4.1. Experiment setup

To validate the proposed method, a hydrodynamic experiment on a circular cylinder under irregular wave actions was performed at the Wind Tunnel and Wave Flume Laboratory, Harbin Institute of Technology in China. The schematic of experiment setup is shown in Fig. 2. In this experiment, a bottom-mounted circular cylinder with a radius of 150 mm was installed in the center of the wave basin. The irregular wave generated by the wave-maker propagated from the right to the left end with a water depth of 0.8 m. JONSWAP spectrum was adopted for generating the random wave field with a period of 1 s. To obtain a more complex multi-direction wave field, four obstructers, which are used to disturb the wave field, were set around the cylinder. To acquire the signals of the wave surface elevation around the cylinder, twelve wave gauges, numbered as shown in Fig. 2, were uniformly distributed around the cylinder, as shown in Fig. 2. To eliminate the effect of the wave gauges on the test model, the supported rod of the sensors was designed to be embedded into the cylinder, and the sensing wire of the wave gauges was installed at the outside with a gap of 5 mm away from the cylinder surface. As shown in Fig. 3, a six-component force balance was embedded in the bottom of the cylinder, and the wave force was transferred to the sensor through the cylinder and the steel keel. During the test, the wave surface elevation and the wave force were recorded at a sampling frequency of 400 Hz. In the following study, the wave force horizontal (F_x and F_y) and base bending moment (M_y and M_x) along the x- and y-direction are mainly considered and discussed. A close-up image of the test model is also depicted in Fig. 3.

4.2. Comparison of the tested and estimated results in the time domain

Under the attack of the random waves, the time history of the wave surface elevation around the cylinder was recorded by the twelve wave gauges. Because of the space limitation, the test data of half wave gauges are shown in Fig. 4 over the
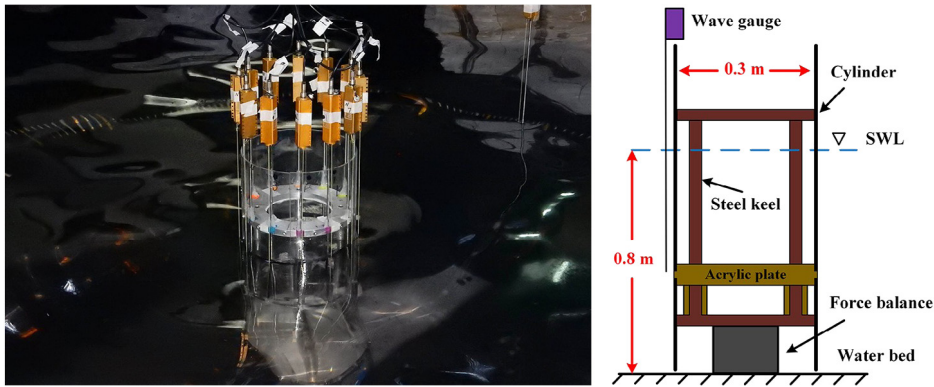
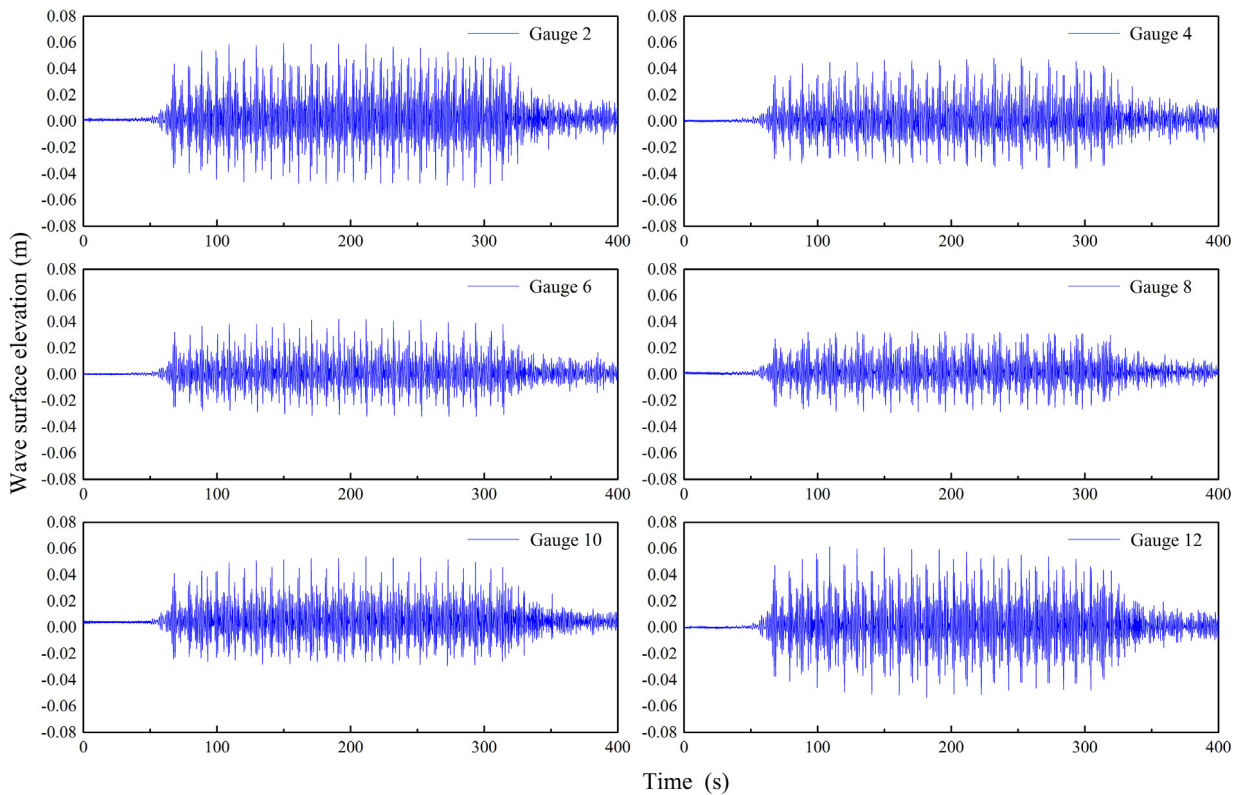**Fig. 3.** Close-up image of the test model in the wave basin.

Fig. 4. Time history of the wave surface elevation around the cylinder recorded by the wave gauges.

time range of 0 ∼ 400 s. In those measured data, the mean values of the signals are extracted from the original data. The wave force and bending moment along the *x*- and *y*-directions were recorded by the force balance simultaneously. Fig. 5 shows a complete signal of the measured horizontal wave force along the *x*-direction. For convenience of analysis, two parts of the signals, named as Region 1 and Region 2 corresponding to the stationary and non-stationary stages, respectively, are separated from the test signal for the following analysis.

To more obviously observe the wave action process, the measured wave elevations (red scatter line) and horizontal wave forces (blue arrow) at four time instances are shown in Fig. 6. For comparison, the SWL is also shown as a gray circle in these figures. The wave force is found to have an obvious correlation with the wave surface elevation. When the wave surface elevation around the cylinder is large at the leading surface, a relative large wave force can also be obtained in the approaching direction, especially in Fig. 6(a) and (d).
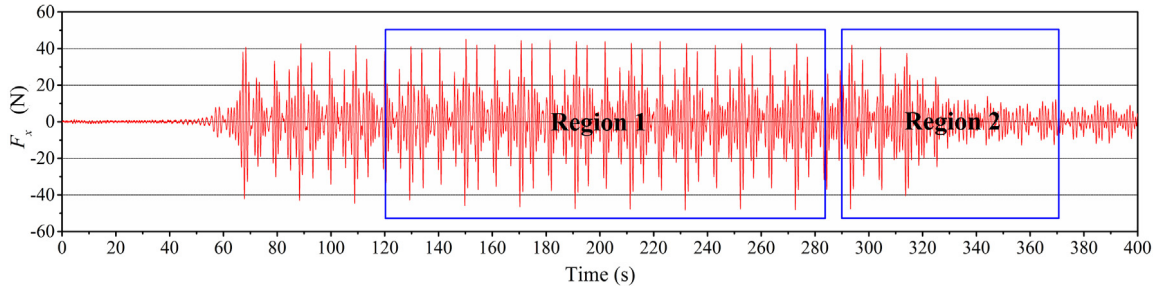
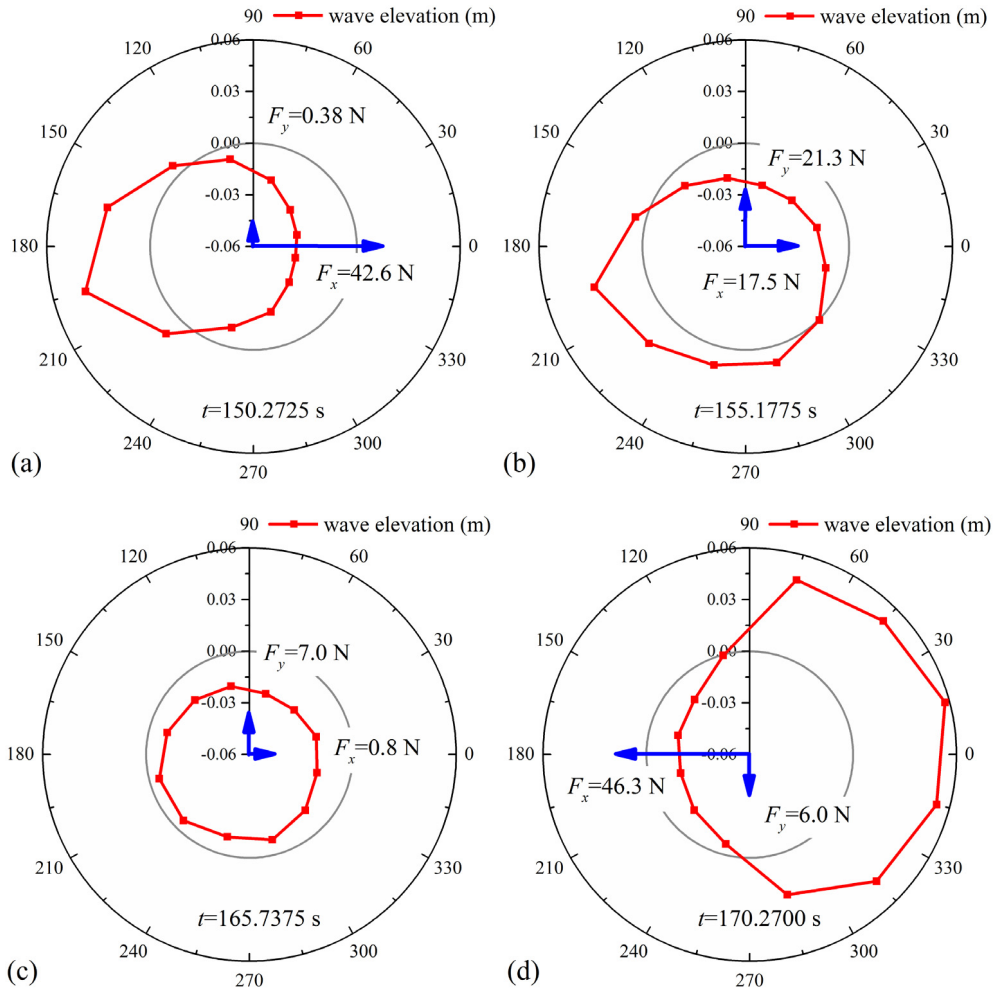**Fig. 5.** Test data of F_x (Region 1: stationary stage; Region 2: non-stationary stage).

Fig. 6. Instantaneous test results of the wave surface elevation around the cylinder and the horizontal wave force: (a) $t = 150.2725$ s; (b) $t = 155.1775$ s; (c) $t = 165.7375$ s; and (d) $t = 170.2700$ s.

Using the proposed method, the horizontal wave forces and base bending moment on the bottom mounted circular cylinder along the two directions are estimated with the data collected by the wave gauges. Taking the signal of Gauge 2 as an example, the calculated $\widetilde{\eta}_F (\pi/4, t)$ and $\widetilde{\eta}_M (\pi/4, t)$ with the scope of [140 s 160s] in stationary region is shown in Fig. 7. To make the data more comparable, the dimensionless values through dividing the max value of themselves, respectively, are adopted in this figure. In addition, the measured signal of the wave gauge in the same region is also depicted in this figure. From Eqs. (50) and (51), it can be found that $\widetilde{\eta}_F$ and $\widetilde{\eta}_M$ have the same phase with η, the calculated $\widetilde{\eta}_F (\pi/4, t)$ and $\widetilde{\eta}_M (\pi/4, t)$ are clearly synchronized well with the measured data.
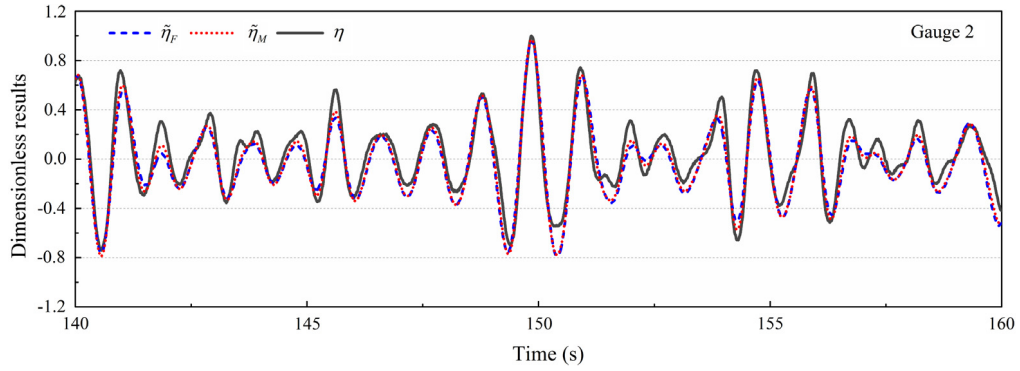
Fig. 7. Time histories for the dimensionless value of $\widetilde{\eta}_F$, $\widetilde{\eta}_M$ and η ($\theta = \pi/4$).

For the circular cylinder, the unit normal vector on the circular cylinder surface is

$$\overrightarrow{\mathbf{n}}_S = \left(\cos\theta \ \ \sin\theta \ \ 0\right) \tag{52}$$

and the unit vector, $\overrightarrow{\mathbf{n}}_0$, in the force direction is

$$\overrightarrow{\mathbf{n}}_0 = \left(\cos\theta_0 \ \ \sin\theta_0 \ \ 0\right) \tag{53}$$

Substituting Eqs. (52) and (53) into Eqs. (27) and (29), the wave force and base bending moment can be obtained as

$$
\begin{aligned}
F\left(\theta_0, t\right) &= -\rho g r_0 \int_0^{2\pi} \widetilde{\eta}_F\left(\theta, t\right) \cos\left(\theta - \theta_0\right) d\theta \\
&= -\rho g r_0 \sum_{n=1}^{12} \widetilde{\eta}_F\left(\theta_n, t\right) \cos\left(\theta_n - \theta_0\right) \Delta\theta
\end{aligned}
\tag{54}
$$

$$
\begin{aligned}
M\left(\theta_0, t\right) &= -\rho g h r_0 \int_0^{2\pi} \widetilde{\eta}_M\left(\theta, t\right) \cos\left(\theta - \theta_0\right) d\theta \\
&= -\rho g h r_0 \sum_{n=1}^{12} \widetilde{\eta}_M\left(\theta_n, t\right) \cos\left(\theta_n - \theta_0\right) \Delta\theta
\end{aligned}
\tag{55}
$$

where r_0 is the radius of the circular cylinder; $\Delta\theta = \pi/6$ and θ_n is

$$\theta_n = \frac{(n-1)\pi}{6} + \frac{\pi}{12}, \ n = 1, 2, \ldots, 12 \tag{56}$$

Based on the above-describe specific conditions for the circular cylinder, the wave force and base bending moment of the test model are estimated by using the measurement of the wave gauges and the proposed method described above. Fig. 8(a) shows the comparison of measured and estimated wave force in the x-direction, F_x, in Region 1 within the time interval of 140–200 s. The figure indicates that the estimated wave force from the measurement of the wave gauges coincides well with the measured wave force by the force balance. Using the same method, the transverse wave force in the y-direction, F_y, is also calculated and depicted in Fig. 8(b) together with the measured wave force by the force balance. The transverse wave force acting on the cylinder is found to be smaller than that in the longitudinal direction.

Similarly, the comparison of M_y and M_x between the estimated and measured results is also shown in Fig. 9. The figure provides evidence that the proposed linear estimation method can also achieve a good result for the base bending moment.

Table 1 shows the statistic results of the measured and estimated wave force and base bending moment in Region 1. The root-of-mean-square (RMS) values of F_x in this region are calculated to be 15.68 N and 15.46 N for the estimated and measured wave forces, respectively, with an error of 1.42%. The corresponding RMS values of F_y are obtained to be 6.98 N and 7.08 N for the estimated and measured wave forces, respectively, with a similar small error of 1.41%. As for the base bending moment, a relative larger estimated errors is found to be 2.88% and 3.36% for M_y and M_x, respectively.

In the non-stationary stage, the proposed method is also utilized to estimate the wave action based on the test results of the wave gauges. Although the recorded data in this region is non-stationary, it can be extended to a period signal through periodic repetition. Therefore, the assumption used in Region 1 can also be used for estimating the wave force of the non-stationary region. Fig. 10 shows the comparison results of the wave force and bending moment in Region 2. Because
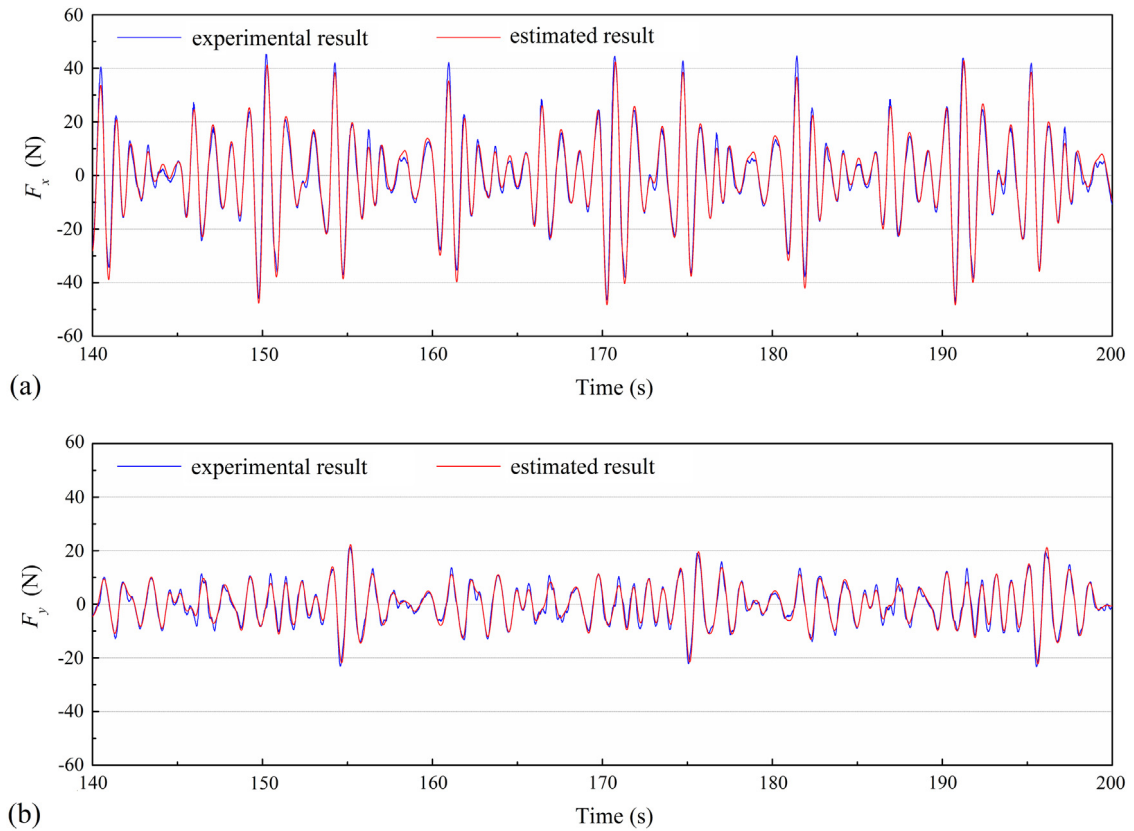
Fig. 8. Comparison between the measured and estimated wave force in Region 1: (a) F_x; and (b) F_y.

Table 1
Comparison between the statistic results of measured and estimated wave action.

Item	Estimated results	Experimental results	Estimated error
F_x	15.68 N	15.46 N	1.42%
F_y	6.98 N	7.08 N	1.41%
M_y	8.77 N · m	9.03 N · m	2.88%
M_x	3.74 N · m	3.87 N · m	3.36%

of the space limitation, only the comparison results of the wave force, F_x, and the bending moment, M_y, are given as examples. The figure shows that a good coincidence can also be found between the results obtained from two different methods. The decay trend of the wave action in transient process can also be effectively estimated using the proposed method.

4.3. Frequency domain and error analysis

To further investigate the error of the linear estimation method, frequency analyses of the estimated and measured wave forces are conducted. Fig. 11(a) shows the power spectral density (PSD) of the tested and estimated results of the horizontal wave force along the x-direction in the stationary region. The PSD of the estimated wave force is observed to approximately overlap with that of the test results. However, some slight differences also exist within the frequency range of [0.7–0.9] Hz. It can also be observed from the comparison of the PSD of the bending moment M_y that the linear estimation method also slightly underestimates the peak value at 1 Hz, as shown in Fig. 11(b). From the above comparison of the measured and estimated wave action, it can be concluded that the proposed linear estimation method is effective for the prediction of the wave force using the wave surface elevation signals around the circular cylinder.

From the above PSD curves, it is also observed the phenomenon that the wave action underestimates the higher-frequency components of the wave force, whereas it overestimates the wave force at the low-frequency region. Although those errors are negligible because of the small energy in those regions compared to that near the dominated frequency,
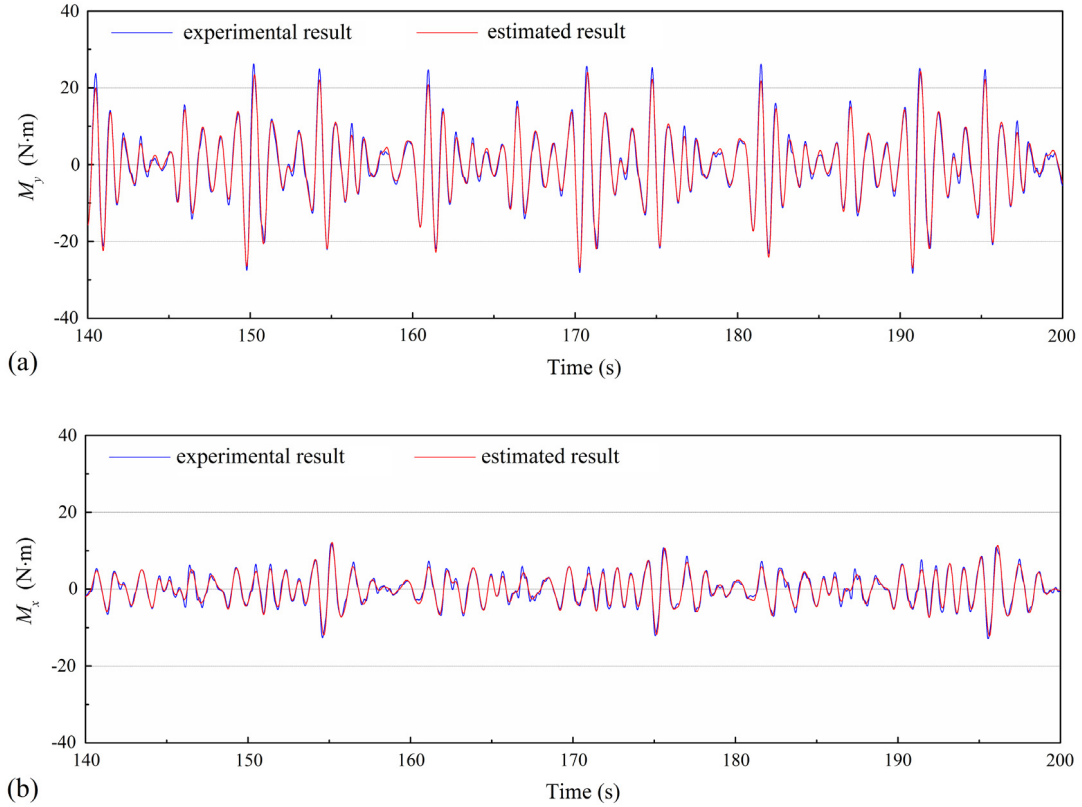
Fig. 9. Comparison between the measured and estimated base bending moment in Region 1: (a) M_y; and (b) M_x.

the reason for this phenomenon is also shown in the following. To more clearly observe the error between the tested and estimated results, the PSDs, as shown in Fig. 11(a), is redrawn in logarithmic coordinate, as shown in Fig. 12.

It is observed from the above derivation that a linear approximation is adopted for calculating the value of $\widetilde{\eta}_F(\theta, t)$ based on the test data of wave gauges. However, it is easily noted that the actual measured wave surface elevation around the cylinder, $\eta(\theta, t)$, by the wave gauges also includes the nonlinear components in terms of the sum frequency and the difference frequency. It can be found that the terms of the sum frequency and the difference frequency in Eq. (40) are actually divided by $\lambda_{\overline{n}}$ rather than α_{nm} to achieve Eq. (50). In this process, errors are introduced because of the linear simplification. To gain insight into this error source, the frequency f_0, which is the sum of f_1 and f_2, is first investigated. According to Eqs. (47) and (B.1), the values of $\lambda_{\overline{n}}$ and α_{nm} can be computed, as shown in Fig. 13(a). In this figure, the blue region denotes the range of values of α_{nm} with a different group of f_1 and f_2, and the red line is the value of $\lambda_{\overline{n}}$. It can be found that the value of α_{nm} is always greater than that of $\lambda_{\overline{n}}$. When α_{nm} is replaced by $\lambda_{\overline{n}}$ in the linear simplification process, it underestimates the wave action because of the effect of the sum term that mainly exists in the higher-frequency region in Fig. 12.

The error induced by the difference frequency term is similar as that of the process of sum frequency term. The difference frequency is given by

$$f_0 = f_1 - f_2 \quad (0 \leq f_2 \leq f_1, f_0 \geq 0) \tag{57}$$

As shown in Fig. 13(b), the values of α_{nm} are always less than those of $\lambda_{\overline{n}}$ as opposed to the sum frequency terms. Therefore, when the linear approximate process replaces α_{nm} by $\lambda_{\overline{n}}$ in the difference frequency term, it would induce the phenomenon of overestimating the wave action in the lower-frequency region, as shown in the left side of Fig. 12. Similar regulation for $\widetilde{\eta}_M(\theta, t)$ can also be found by using the same method for the coefficients of $(\vartheta_{\overline{n}} + \lambda_{\overline{n}})$ and $(\beta_{nm} + \alpha_{nm})$, as shown in Fig. 14. Therefore, it can be concluded that the linear approximate method proposed in this study would underestimate the sum frequency term and overestimate the difference frequency term for both wave force and wave bending moment.

During the derivation of in Eqs. (27) and (29), the effect of coefficient $\delta_{nm}(\eta)$ and $\sigma_{nm}(\eta)$ are neglected, which also induces error of the estimated wave action. To analyze the effects of this simplification, error analysis is also conducted regarding this issue. However, note that the formulation of $\delta_{nm}(\eta)$ and $\sigma_{nm}(\eta)$ containing the unknown function of $g_n \cdot g_m$ are complex and difficult to obtain from the information of the measured wave surface elevation by the wave gauges. To evaluate the
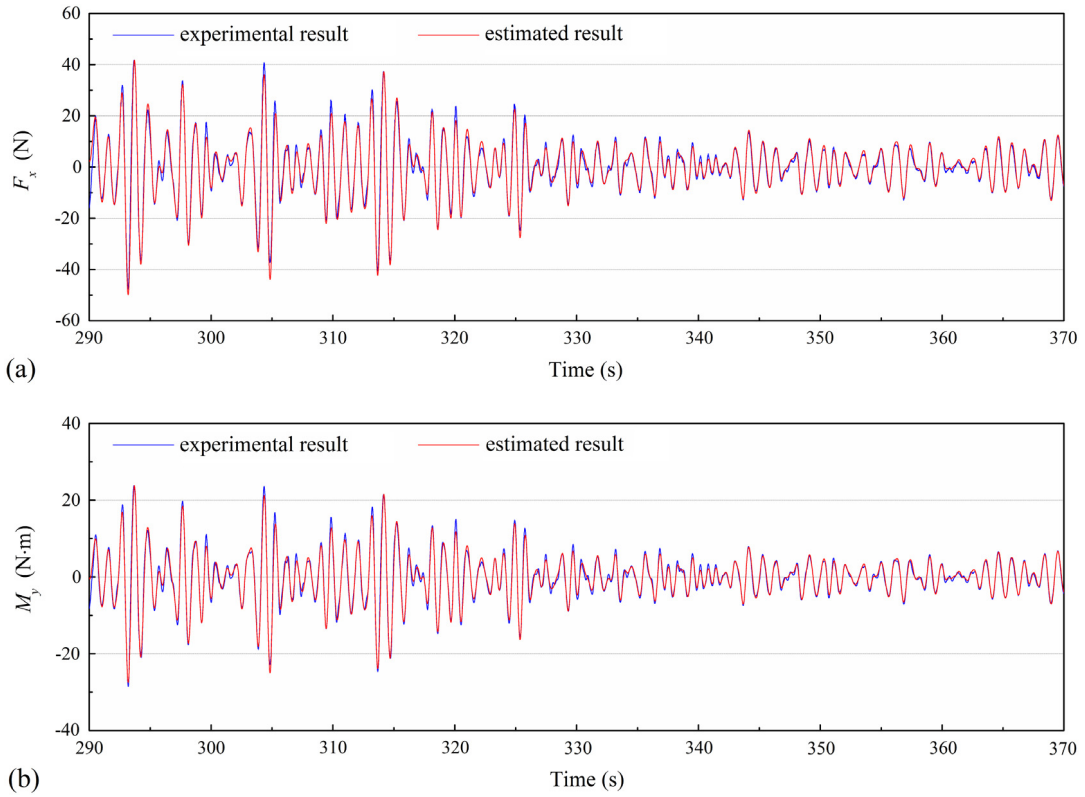
Fig. 10. Comparison of the wave action along the longitudinal direction in Region 2: (a) F_x; and (b) M_y.
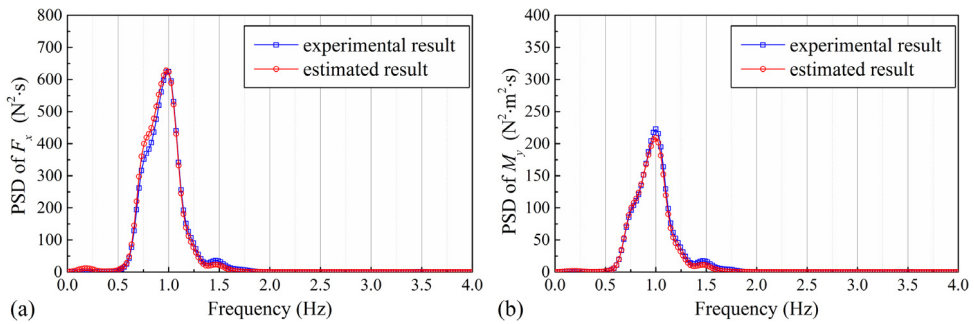

Fig. 11. PSDs of the wave force and bending moment in the stationary region: (a) F_x; and (b) M_y.
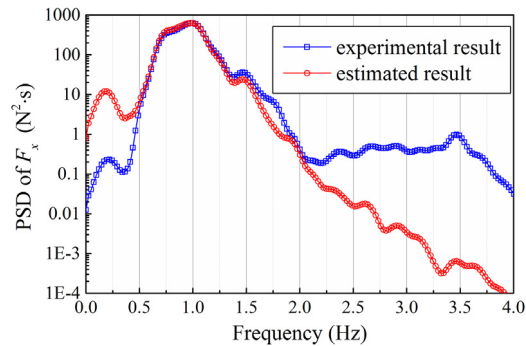

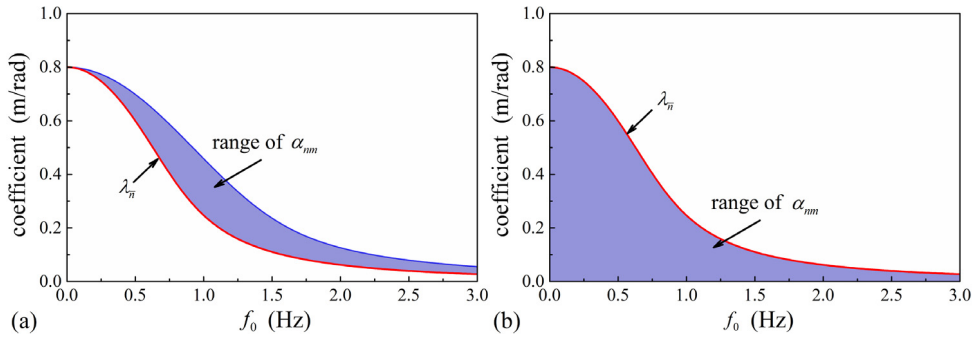**Fig. 12.** PSD of F_x in stationary region with logarithmic coordinate.

Fig. 13. Error analysis for the coefficients of $\lambda_{\bar{n}}$ and α_{nm}: (a) Sum frequency; and (b) difference frequency.
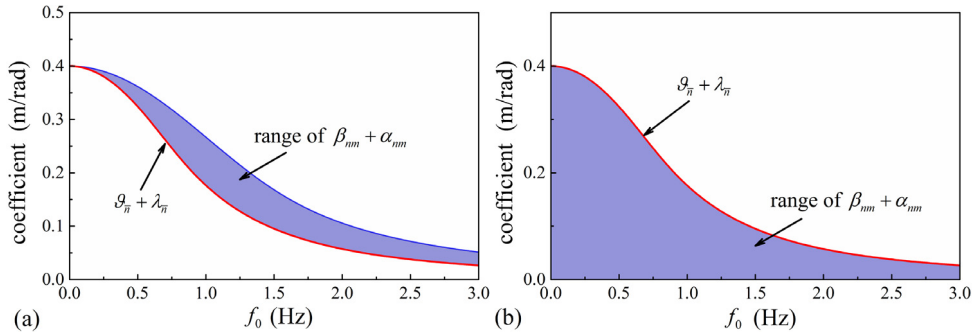

Fig. 14. Error analysis for the coefficients of $(\vartheta_{\bar{n}} + \lambda_{\bar{n}})$ and $(\beta_{nm} + \alpha_{nm})$: (a) Sum frequency; and (b) difference frequency.

effect of $\delta_{nm}(\eta)$, an error function is defined as following:

$$E_\delta = \left\| \frac{\delta_{nm}(\eta)}{g_n g_m k_n k_m \dot{f}_n(k_n \eta) \dot{f}_m(k_m \eta) \alpha_{nm}(\eta)} \right\|_{\eta=0} \tag{58}$$

where the denominator of E_δ is part of $\zeta_{nm}(\theta, t) \alpha_{nm}(\eta)$ in Eq. (A.2) of Appendix A.

For the frequency groups (f_1, f_2) of two arbitrary superimposed wave, the error function is calculated and shown in Fig. 15(a). As shown in the figure, the values of E_δ are higher when the frequency groups close to zeros, i.e., the effect becomes more significant for the waves with long period.

Similarly, an error function for $\sigma_{nm}(\eta)$ can also be defined as

$$E_\sigma = \left\| \frac{\sigma_{nm}(\eta)}{g_n g_m k_n k_m \dot{f}_n(k_n \eta) \dot{f}_m(k_m \eta) \beta_{nm}(\eta)} \right\|_{\eta=0} \tag{59}$$

where the denominator of E_σ is part of $\zeta_{nm}(\theta, t) \beta_{nm}(\eta)$, as shown in Eq. (A.3) of the Appendix. Likewise, the relationship between E_σ and frequency group (f_1, f_2) are also calculated and shown in Fig. 15(b). The same conclusion can be found from this figure. When the nonlinear part of wave action is very small, the error can be neglected; even the values of E_δ and E_σ reach to 0.65 and 0.80, respectively. It can also be found from Fig. 15 that the effects of $\delta_{nm}(\eta)$ and $\sigma_{nm}(\eta)$ for the case of frequency group with small wave periods is very small. However, when the nonlinearity is very strong, the effects of coefficient $\delta_{nm}(\eta)$ and $\sigma_{nm}(\eta)$ on the wave force estimation should be further investigated for such cases.

5. Conclusions

This paper presented a methodology to estimate the wave action on rigid bottom-mounted cylinders using the monitoring information of wave surface elevation around the structure surface. Formulas are derived based on the potential theory, and a hydrodynamic experiment was performed on circular cylinder to validate the proposed method. The major conclusions include:

(1) There is an inherent relationship between the wave surface elevation around the bottom-mounted cylinders and the wave loads acting on the structure. The classic potential theory can be used to estimate the wave force on the cylinder without the need to know the velocity potential of the whole wave field.
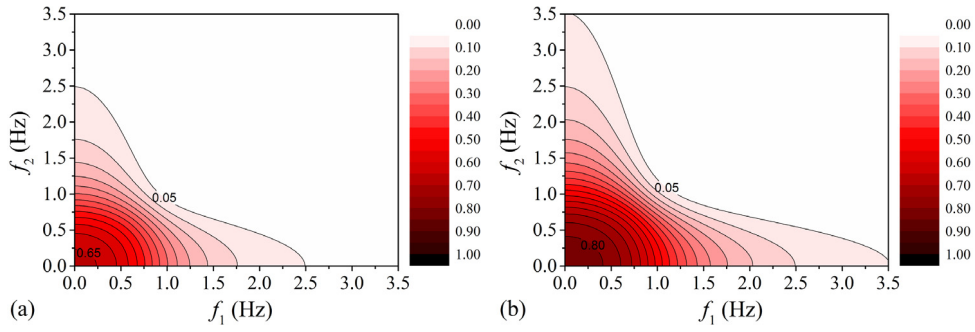
Fig. 15. Error analysis for the coefficients. (a) E_δ; (b) E_σ.

(2) The formulae of the proposed method are derived in a general way. Considering the difficulty of including all of the nonlinear terms in the estimation process, a linear approximate method is proposed from a simplified integral formula of wave surface elevation. The test results demonstrated that the approximate method can also achieve a good estimation of the wave loads on the cylinders.

(3) The error induced by the simplification can be explained from the frequency domain analysis of the function of the concerned coefficients. The linear estimation method slightly underestimates sum frequency term, whereas it overestimates the difference frequency term.

This study provides a possible novel approach for real-time monitoring the wave loads acting on the bottom-mounted cylinders using the wave surface elevation around the coastal cylindrical structure. Although the experiment was conducted on a circular cylinder, it can also be used for predicting the wave loads of rigid bottom-mounted cylinder with arbitrary cross sections. As a pioneering investigation, further study is still required on this topic in the future, such as:

(1) Use fewer wave gauges to obtain acceptable estimated results, and analyze the effect of location of wave gauges on the estimated results;

(2) Develop a nonlinear estimation method that include the sum frequency and difference frequency terms to obtain more accurate results.

Acknowledgments

Appendix A

The detailed derivation of Eq. (7) is given as follows:

$$
\begin{aligned}
M_0(\theta_0, t) &= \int_{S=0} \int_{-h}^{\eta(\theta,t)} P(h+z)\left(-\vec{\mathbf{n}}_S\right) \cdot \vec{\mathbf{n}}_0 dzds = \int_0^{2\pi} \int_{-h}^{\eta(\theta,t)} P(h+z)\left(-\vec{\mathbf{n}}_S\right) \cdot \vec{\mathbf{n}}_0 \cdot \tilde{r}(\theta) dzd\theta \\
&= \int_0^{2\pi} \int_{-h}^{\eta(\theta,t)} \left(-\rho g z(h+z) - \rho(h+z)\,\mathrm{Re}\left\{\frac{\partial\Phi}{\partial t}\right\}\right. \\
&\quad \left. -\frac{\rho}{2}(h+z)\,\mathrm{Re}\left\{\nabla\Phi\right\}\cdot\mathrm{Re}\left\{\nabla\Phi\right\}\right)\Bigg|_{S=0} \left(-\vec{\mathbf{n}}_S\right) \cdot \vec{\mathbf{n}}_0 \cdot \tilde{r}(\theta) dzd\theta \\
&= \int_0^{2\pi} \int_{-h}^{\eta(\theta,t)} \left(-\rho z\,\mathrm{Re}\left\{\frac{\partial\Phi}{\partial t}\right\} - \frac{\rho}{2}z\,\mathrm{Re}\left\{\nabla\Phi\right\}\cdot\mathrm{Re}\left\{\nabla\Phi\right\}\right)\Bigg|_{S=0} \left(-\vec{\mathbf{n}}_S\right) \cdot \vec{\mathbf{n}}_0 \cdot \tilde{r}(\theta) dzd\theta \\
&\quad + F_0(\theta_0, t)\,h \\
&= M_\xi(\theta_0, t) + M_\zeta(\theta_0, t) + F_0(\theta_0, t)\,h
\end{aligned}
\tag{A.1}
$$

where $M_\xi(\theta_0, t)$ and $M_\zeta(\theta_0, t)$ are shown in Eq. (10) and (11), respectively.

The detailed derivation of Eq. (21) is given as follows:

$$
\begin{aligned}
F_\zeta \left(\theta, t\right) &= \int_0^{2\pi} \int_{-h}^{\eta(\theta,t)} \left(-\frac{\rho}{2} \text{Re}\left\{\nabla\Phi\right\} \cdot \text{Re}\left\{\nabla\Phi\right\} \right)\Big|_{S=0} \left(-\overrightarrow{\mathbf{n}}_S\right) \cdot \overrightarrow{\mathbf{n}}_0 \cdot \widetilde{r}(\theta)dzd\theta \\
&= \sum_{n=1}^{\infty}\sum_{m=1}^{\infty} -\frac{\rho}{2} \int_0^{2\pi} \int_{-h}^{\eta(\theta,t)} \left\{ f_n f_m (g_n)'_r (g_m)'_r + \frac{f_n f_m}{r^2}(g_n)'_\theta (g_m)'_\theta \right. \\
&\quad \left. + g_n g_m k_n k_m \dot{f}_n \dot{f}_m \right\} \left(-\overrightarrow{\mathbf{n}}_S\right) \cdot \overrightarrow{\mathbf{n}}_0 \cdot \widetilde{r}(\theta)dzd\theta \\
&= \sum_{n=1}^{\infty}\sum_{m=1}^{\infty} -\frac{\rho}{2} \int_0^{2\pi} \left\{ (g_n)'_r (g_m)'_r \int_{-h}^{\eta(\theta,t)} f_n f_m dz + \frac{(g_n)'_\theta (g_m)'_\theta}{r^2} \int_{-h}^{\eta(\theta,t)} f_n f_m dz \right. \\
&\quad \left. + g_n g_m k_n k_m \int_{-h}^{\eta(\theta,t)} \dot{f}_n \dot{f}_m dz \right\} \left(-\overrightarrow{\mathbf{n}}_S\right) \cdot \overrightarrow{\mathbf{n}}_0 \cdot \widetilde{r}(\theta)d\theta \\
&= \sum_{n=1}^{\infty}\sum_{m=1}^{\infty} -\frac{\rho}{2} \int_0^{2\pi} \left\{ \left[f_n(\eta)f_m(\eta)(g_n)'_r (g_m)'_r + \frac{f_n(\eta)f_m(\eta)(g_n)'_\theta (g_m)'_\theta}{r^2} \right. \right. \\
&\quad \left. \left. + g_n g_m k_n k_m \dot{f}_n(k_n\eta)\dot{f}_m(k_m\eta) \right] \alpha_{nm}(\eta) + \delta_{nm}(\eta) \right\} \left(-\overrightarrow{\mathbf{n}}_S\right) \cdot \overrightarrow{\mathbf{n}}_0 \cdot \widetilde{r}(\theta)d\theta \\
&= \sum_{n=1}^{\infty}\sum_{m=1}^{\infty} \rho g \int_0^{2\pi} \left\{\zeta_{nm}\left(\theta, t\right)\alpha_{nm}(\eta) + \delta_{nm}(\eta)\right\} \left(-\overrightarrow{\mathbf{n}}_S\right) \cdot \overrightarrow{\mathbf{n}}_0 \cdot \widetilde{r}(\theta)d\theta
\end{aligned}
\tag{A.2}
$$

where $\alpha_{nm}(\eta)$ and $\delta_{nm}(\eta)$ are shown in Eqs. (23) and (24), respectively.

The detailed derivation of Eq. (22) is given as follows:

$$
\begin{aligned}
M_\zeta \left(\theta, t\right) &= \int_0^{2\pi} \int_{-h}^{\eta(\theta,t)} \left(-\frac{\rho z}{2} \text{Re}\left\{\nabla\Phi\right\} \cdot \text{Re}\left\{\nabla\Phi\right\} \right)\Big|_{S=0} \left(-\overrightarrow{\mathbf{n}}_S\right) \cdot \overrightarrow{\mathbf{n}}_0 \cdot r(\theta)dzd\theta \\
&= \sum_{n=1}^{\infty}\sum_{m=1}^{\infty} -\frac{\rho}{2} \int_0^{2\pi} \int_{-h}^{\eta(\theta,t)} \left\{ z f_n f_m (g_n)'_r (g_m)'_r + z\frac{f_n f_m}{r^2}(g_n)'_\theta (g_m)'_\theta \right. \\
&\quad \left. + z g_n g_m k_n k_m \dot{f}_n \dot{f}_m \right\} \left(-\overrightarrow{\mathbf{n}}_S\right) \cdot \overrightarrow{\mathbf{n}}_0 \cdot \widetilde{r}(\theta)dzd\theta \\
&= \sum_{n=1}^{\infty}\sum_{m=1}^{\infty} -\frac{\rho}{2} \int_0^{2\pi} \left\{ (g_n)'_r (g_m)'_r \int_{-h}^{\eta(\theta,t)} z f_n f_m dz + \frac{(g_n)'_\theta (g_m)'_\theta}{r^2} \int_{-h}^{\eta(\theta,t)} z f_n f_m dz \right. \\
&\quad \left. + g_n g_m k_n k_m \int_{-h}^{\eta(\theta,t)} z \dot{f}_n \dot{f}_m dz \right\} \left(-\overrightarrow{\mathbf{n}}_S\right) \cdot \overrightarrow{\mathbf{n}}_0 \cdot \widetilde{r}(\theta)d\theta \\
&= \sum_{n=1}^{\infty}\sum_{m=1}^{\infty} -\frac{\rho}{2}h \int_0^{2\pi} \left\{ \left[f_n(\eta)f_m(\eta)(g_n)'_r (g_m)'_r + \frac{f_n(\eta)f_m(\eta)(g_n)'_\theta (g_m)'_\theta}{r^2} \right. \right. \\
&\quad \left. \left. + g_n g_m k_n k_m \dot{f}_n(k_n\eta)\dot{f}_m(k_m\eta) \right] \beta_{nm}(\eta) + \sigma_{nm}(\eta) \right\} \left(-\overrightarrow{\mathbf{n}}_S\right) \cdot \overrightarrow{\mathbf{n}}_0 \cdot \widetilde{r}(\theta)d\theta \\
&= \sum_{n=1}^{\infty}\sum_{m=1}^{\infty} \rho g h \int_0^{2\pi} \left\{\zeta_{nm}\left(\theta, t\right)\beta_{nm}(\eta) + \sigma_{nm}(\eta)\right\} \left(-\overrightarrow{\mathbf{n}}_S\right) \cdot \overrightarrow{\mathbf{n}}_0 \cdot \widetilde{r}(\theta)d\theta
\end{aligned}
\tag{A.3}
$$

where $\beta_{nm}(\eta)$ and $\sigma_{nm}(\eta)$ are shown in Eqs. (25) and (26), respectively.

Appendix B

The formulae for $\alpha_{nm}(\eta)$ and $\beta_{nm}(\eta)$ are

$$
\begin{aligned}
\alpha_{nm}(\eta) &= \frac{\frac{1}{k_n+k_m}\sinh(k_n+k_m)(\eta+h) + \frac{1}{k_n-k_m}\sinh(k_n-k_m)(\eta+h)}{\cosh(k_n+k_m)(\eta+h) + \cosh(k_n-k_m)(\eta+h)} \\
&\approx \frac{\frac{1}{k_n+k_m}\sinh(k_n+k_m)h + \frac{1}{k_n-k_m}\sinh(k_n-k_m)h}{\cosh(k_n+k_m)h + \cosh(k_n-k_m)h}
\end{aligned}
\tag{B.1}
$$

$$\beta_{nm}(\eta) = \frac{\frac{1}{h}\left\{\begin{array}{l}\frac{1}{k_n + k_m}\left\{\eta \sinh\left(k_n + k_m\right)\left(\eta + h\right) - \frac{1}{\left(k_n + k_m\right)}\left(\cosh\left(k_n + k_m\right)\left(\eta + h\right) - 1\right)\right\} + \\ \frac{1}{k_n - k_m}\left\{\eta \sinh\left(k_n - k_m\right)\left(\eta + h\right) - \frac{1}{\left(k_n - k_m\right)}\left(\cosh\left(k_n - k_m\right)\left(\eta + h\right) - 1\right)\right\}\end{array}\right\}}{\cosh\left(k_n + k_m\right)\left(\eta + h\right) + \cosh\left(k_n - k_m\right)\left(\eta + h\right)}$$
$$\approx \frac{\frac{1}{h(k_n + k_m)^2}\left(1 - \cosh\left(k_n + k_m\right)h\right) + \frac{1}{h(k_n - k_m)^2}\left(1 - \cosh\left(k_n - k_m\right)h\right)}{\cosh\left(k_n + k_m\right)h + \cosh\left(k_n - k_m\right)h} \tag{B.2}$$

References

Boccotti, P., Arena, F., Fiamma, V., Barbaro, G., 2012. Field experiment on random wave forces acting on vertical cylinders. Probabilist. Eng. Mech. 28, 39–51.

Borthwick, A.G.L., 1989. Pressure and force measurements on a cylinder oscillated sinusoidally at low and intermediate keulegan-carpenter numbers. J. Fluids Struct. 3 (5), 509–528.

Burrows, R., Tickell, R.G., Hames, D., Najafian, G., 1997. Morison wave force coefficients for application to random seas. Appl. Ocean Res. 19 (3), 183–199.

Chan, E.S., Cheong, H.F., Tan, B.C., 1995. Laboratory study of plunging wave impacts on vertical cylinders. Coast. Eng. 25 (1–2), 87–107.

De Vos, L., Frigaard, P., De Rouck, J., 2007. Wave run-up on cylindrical and cone shaped foundations for offshore wind turbines. Coast. Eng. 54 (1), 17–29.

Deng, Y., Yang, J., Zhao, W., Li, X., Xiao, L., 2016. Freak wave forces on a vertical cylinder. Coast. Eng. 114, 9–18.

Hosseinlou, F., Mojtahedi, A., 2016. Developing a robust simplified method for structural integrity monitoring of offshore jacket-type platform using recorded dynamic responses. Appl. Ocean Res. 56, 107–118.

Isaacson, M., 1979. Wave-induced forces in the diffraction regime. In: Shaw, T.L. (Ed.), Mechanics of Wave-Induced Forces on Cylinders. Pitman Publishing, Ltd., London, pp. 68–89.

Jamalkia, A., Ettefagh, M.M., Mojtahedi, A., 2016. Damage detection of TLP and spar floating wind turbine using dynamic response of the structure. Ocean Eng. 125, 191–202.

Keulegan, G.H., Carpenter, L.H., 1956. Forces on cylinders and plates in an oscillating fluid. J. Res. Natl. Bur. Stand. 60, 432–440.

Li, J., Wang, Z., Liu, S., 2012. Experimental study of interactions between multi-directional focused wave and vertical circular cylinder, Part I : wave run-up. Coast. Eng. 64, 151–160.

Li, J., Wang, Z., Liu, S., 2014. Experimental study of interactions between multi-directional focused wave and vertical circular cylinder, Part II : wave force. Coast. Eng. 83, 233–242.

Li, Y.S., Zhan, S., Lau, S.L.L., 1997. In-line response of a horizontal cylinder in regular and random waves. J. Fluids Struct. 11 (1), 73–87.

Lotfollahi-Yaghin, M.A., Pourtaghi, A., Sanaaty, B., Lotfollahi-Yaghin, A., 2012. Artificial neural network ability in evaluation of random wave-induced inline force on a vertical cylinder. China Ocean Eng. 26 (1), 19–36.

MacCamy, R., Fuchs, R., 1954. Wave forces on piles: A diffraction theory, Technical Memo., US Army Board, US Army Corp. Eng.

Martinez-Luengo, M., Kolios, A., Wang, L., 2016. Structural health monitoring of offshore wind turbines: A review through the statistical pattern recognition paradigm. Renew. Sust. Energ. Rev. 64, 91–105.

Mojtahedi, A., et al., 2011. Developing a robust shm method for offshore jacket platform using model updating and fuzzy logic system. Appl. Ocean Res. 33 (4), 398–411.

Morison, J.R., Johnson, J.W., Schaaf, S.A., 1950. The force exerted by surface waves on piles. 189, pp. 149-56.

Niedzwecki, J.M., Duggal, A.S., 1992. Wave runup and forces on cylinders in regular and random waves. J. Waterway, Port, Coastal, Ocean Eng. 118 (6), 615–634.

Sarpkaya, T., 2010. Wave Forces on Offshore Structures. Cambridge University Press, New York, USA.

Tung, C.C., 1996. Total wave force on cylinder considering free surface fluctuation. Appl. Ocean Res. 18 (1), 37–43.